Acta Mechanica 128, 49–58 (1998)

ACTA MECHANICA

Numerical investigation of viscous flow over a hemisphere-cylinder

R. C. Mehta, Trivandrum, India

(Received October 15, 1996; revised December 9, 1996)

Summary. A numerical analysis has been performed to investigate turbulent compressible flow over a hemisphere-cylinder body at zero incidence in the Mach number range of 0.8–2.0. The numerical code solves the Navier-Stokes equations using finite volume technique in conjunction with multistage Runge-Kutta time-stepping method. Comparisons have been made with the available experimental data such as shadowgraph pictures, shock stand-off distance, shock position and surface pressure distribution. They are found in good agreement. A separated flow on the hemisphere-cylinder junction is noticed between Mach numbers 0.8 and 0.9. It is observed from the velocity vector plots that the flow appears to become parallel to the body in the vicinity of the stagnation point of the hemisphere at supersonic Mach number.

Nomenclature

C_P	pressure coefficient
C_p	specific heat at constant pressure
e	total energy per unit mass
$\boldsymbol{F}, \boldsymbol{G}, \boldsymbol{H}$	flux vectors
$\boldsymbol{i}, \boldsymbol{j}$	unit vectors in (x, r) directions
M	Mach number
$\boldsymbol{n}$	unit normal vector
Pr	Prandtl number
$\mathbf{Q}$	flux tensor
q	heat flux vector
R	cylinder radius
T	temperature
t	time
u, v	velocity components in (x, r) directions
$\boldsymbol{W}$	vector of conserved variables
x, r	coordinate directions
Δ	shock stand-off distance
γ	ratio of specific heats
μ	viscosity
ϱ	density
σ	stress tensor

Subscripts

t	turbulent
w	wall
∞	freestream condition

1 Introduction

The design process for aerospace application has been improved significantly by the use of computational fluid dynamics. Numerical solutions of the Navier-Stokes equations have been used to obtain a better understanding of the qualitative and quantitative physical phenomena in steady viscous flows. The application of a hemisphere-cylinder is one of the basic nose configurations for blunt nose bodies of revolution. A detailed analysis of the phenomena of viscous flow will reveal the physical features of transonic and supersonic flow over nose-bodies in general.

Hsieh [1] has conducted wind-tunnel tests of a hemisphere-cylinder model at zero incidence and Mach number range of $0.7-1.3$ in order to investigate viscous-inviscid interaction of flow field. Hsieh [2] has solved the full potential equation to analyse experimental data and found that the inviscid analysis is unable to predict the external flow field satisfactorily. This is due to the fact that the shock wave-boundary layer interaction causes a separated flow between Mach number $0.8-0.9$ on the junction of hemisphere-cylinder.

In the present paper, the Reynolds-averaged turbulent compressible Navier-Stokes equations are solved using finite volume discretization in conjunction with multistage Runge-Kutta time-marching method. Turbulence closure is achieved using an algebraic turbulence model. The numerical results of the present analysis are compared with the available experimental data. An interesting flow field phenomenon is observed in the vicinity of the stagnation point of the hemisphere and is discussed.

2 Numerical analysis

2.1 Governing equations

The time-dependent axisymmetric Reynolds-averaged Navier-Stokes equations can be written in integral form as

$$\frac{d}{dt}\int_V \boldsymbol{W}\,dV + \int_S \boldsymbol{Q}\cdot\boldsymbol{n}\,dS + \int_V \boldsymbol{H}\,dV = 0 \tag{1}$$

where $\boldsymbol{W} = r[\varrho, \varrho u, \varrho v, \varrho e]^T$, $\boldsymbol{Q} = (\boldsymbol{F}.\boldsymbol{i} + \boldsymbol{G}.\boldsymbol{j})$, $\boldsymbol{H}$ is a source term, and S surrounds the volume V. The vectors $\boldsymbol{F}$, $\boldsymbol{G}$, and $\boldsymbol{H}$ are given by

$$\boldsymbol{F} = r[\varrho u, \varrho u^2 + p - \sigma_{xx}, \varrho uv - \sigma_{xr}, (\varrho e + p - \sigma_{xx})\,u - v\sigma_{xr} + q_x]^T \tag{2.1}$$

$$\boldsymbol{G} = r[\varrho v, \varrho uv - \sigma_{xr}, \varrho v^2 + p - \sigma_{rr}, (\varrho e + p - \sigma_{rr})\,v - u\sigma_{xr} + q_r]^T \tag{2.2}$$

$$\boldsymbol{H} = [0, 0, -p + \sigma_{\theta\theta}, 0]^T \tag{2.3}$$

where $\sigma_{xx}, \sigma_{xr}, \sigma_{rr}, \sigma_{\theta\theta}$ are components of the stress vectors, while q_x and q_r are components of heat flux vectors. Reynolds stresses and turbulent heat fluxes in the mean flow equations are modeled by introducing an isotropic eddy viscosity μ_t and turbulent Prandtl number Pr_t. Thus, the viscous

terms in Eqs. (2) can be written as

$$\sigma_{xx} = (\mu + \mu_t)\left[\frac{4}{3}\frac{\partial u}{\partial x} - \frac{2}{3}\left(\frac{\partial v}{\partial r} + \frac{v}{r}\right)\right]$$

$$\sigma_{xr} = (\mu + \mu_t)\left[\frac{\partial u}{\partial r} + \frac{\partial v}{\partial x}\right]$$

$$\sigma_{rr} = (\mu + \mu_t)\left[\frac{4}{3}\frac{\partial v}{\partial r} - \frac{2}{3}\left(\frac{\partial u}{\partial x} + \frac{v}{r}\right)\right]$$

$$\sigma_{\theta\theta} = (\mu + \mu_t)\left[\frac{4}{3}\frac{v}{r} - \frac{2}{3}\left(\frac{\partial u}{\partial x} + \frac{\partial v}{\partial r}\right)\right]$$

$$q_x = -C_P\left(\frac{\mu}{\mathrm{Pr}} + \frac{\mu_t}{\mathrm{Pr}_t}\right)\frac{\partial T}{\partial x}$$

$$q_r = -C_P\left(\frac{\mu}{\mathrm{Pr}} + \frac{\mu_t}{\mathrm{Pr}_t}\right)\frac{\partial T}{\partial r}.$$

The temperature is obtained from the equation of state,

$$p = (\gamma - 1)\,\varrho T, \tag{3}$$

and

$$\varrho e = \frac{p}{(\gamma - 1)} + \frac{1}{2}\,\varrho(u^2 + v^2). \tag{4}$$

For the turbulent flow situation, the closure of the system of equations is achieved by introducing the turbulence model of Baldwin-Lomax [3].

2.2 Numerical algorithm

The code uses the finite-volume discretization procedure. The computational domain is divided into a number of quadrilateral cells. Flow variables are stored at cell centres, and the flux balancing reduces to a contour integral around the perimeter of each cell. This essentially gives a conservative central differencing scheme that is second-order accurate on smoothly varying grids. First derivatives are required at the centre of the cell sides to evaluate the stress and heat flux terms.

Artificial dissipation is added to Eq. (1) to eliminate undamped modes and to capture shocks without pre-shock oscillations. Following Jamesons et al. [4], a combination of second and fourth differences is employed, with the second difference being controlled by a pressure sensor.

Temporal integration is performed by the three-stage method of Jamesons et al. [4] based on the Runge-Kutta scheme. The numerical scheme is stable for a Courant number $\leqq 2$. Local time steps are used to accelerate convergence to a steady state solution by advancing the time step at each grid point with the maximum permissible able time step allowed by the local CFL condition.

2.3 Boundary conditions

Four types of boundary conditions are required for the computation of the flow field, i.e., inflow, wall, outflow and symmetric conditions. They are described as follows:

At the inflow, all flow variables are prescribed at free stream conditions. On the impermeable wall, the no-slip condition for the velocity is taken as

$$u_w = v_w = 0 \tag{5}$$

together with the adiabatic wall condition.

For the subsonic flow, non-reflecting far field boundary conditions are applied at the outer boundary of the computational domain. For supersonic case, all the flow variables are extrapolated at the outflow from the vector of conserved variables $\boldsymbol{W}$ as

$$\boldsymbol{W}_{nx,j} = \boldsymbol{W}_{nx-1,j} - \boldsymbol{W}_{nx-2,j} \tag{6.1}$$

$$\boldsymbol{W}_{i,nr} = \boldsymbol{W}_{i,nr-1} - \boldsymbol{W}_{i,nr-2} \tag{6.2}$$

where the subscripts nx and nr represent the last grid points on the boundaries.

For the symmetric condition, the centre-line requires the following conditions:

$$\varrho v = 0 \tag{7.1}$$

$$\frac{\partial u}{\partial r} = \frac{\partial T}{\partial r} = \frac{\partial p}{\partial r} = 0. \tag{7.2}$$

2.4 Computational grid

The physical space is discretized into a number of nonuniformly spaced grid points. The body oriented grids are generated by a homotopy scheme [5]. The hemisphere-cylinder space is defined by a number of grid points in cylindrical polar coordinates. Using these surface points as reference mesh points, the normal coordinates are then obtained by exponentially stretched grid points extending outwards upto an outer boundary.

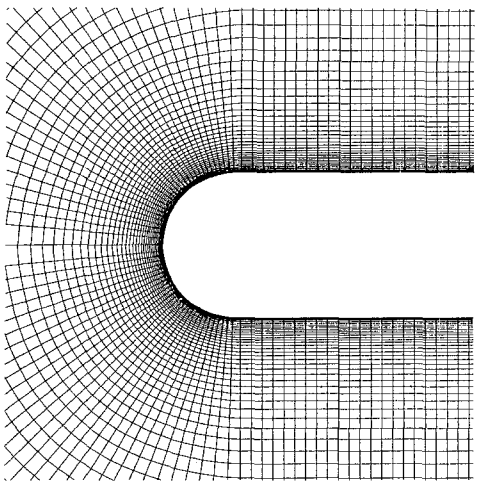

Fig. 1. Enlarged view of grid

The grid independent test cases are carried out taking into consideration the effect of the computational domain, stretching factor to control the grid intensity near the wall, number of grid points in the axial and normal directions. The dimension of the hemisphere-cylinder model [1] is taken as 2.54×10^{-2} m diameter and 25.4×10^{-2} m length. The outer boundary of the computational domain is varied from 5 to 12 times the cylinder diameter. The blockage ratio is found in the range of 4 to 0.7%, which is defined as the ratio of cross-sectional area of the model to the computational domain. The stretching factor is varied from 1.5 to 5.

The computation used 120×52 grid points in the axial and radial directions, respectively. The stretching factor is selected 4.5, and the computational domain is kept 12 times the cylinder diameter. This grid arrangement is found to yield a grid independent result. Figure 1 depicts a close-up view of the grid employed in the numerical simulation.

3 Results and discussion

The numerical procedure described in the previous Section is applied here to compute the flow field over a hemisphere-cylinder. Figure 2 depicts the velocity field on the hemisphere-cylinder at free stream Mach number of 0.8 and 0.9. A separation bubble can be seen on the junction of

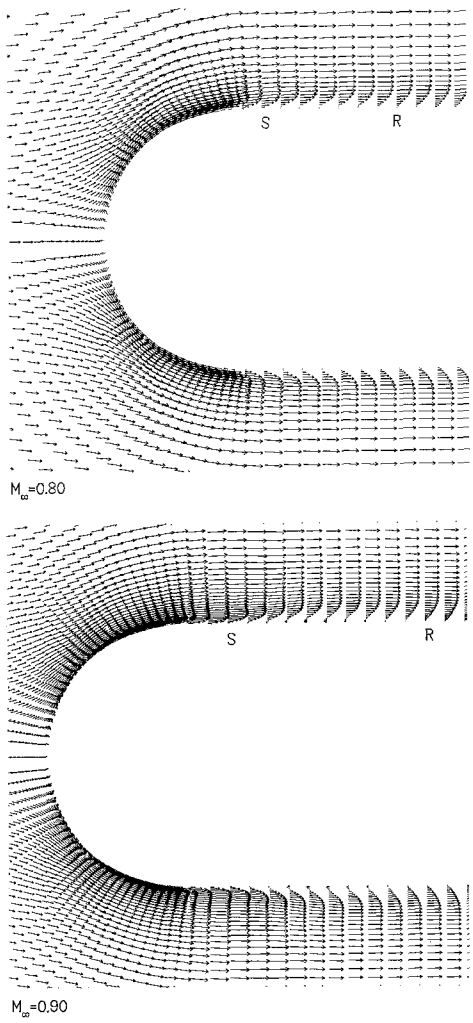

Fig. 2. Vector plots over hemisphere-cylinder

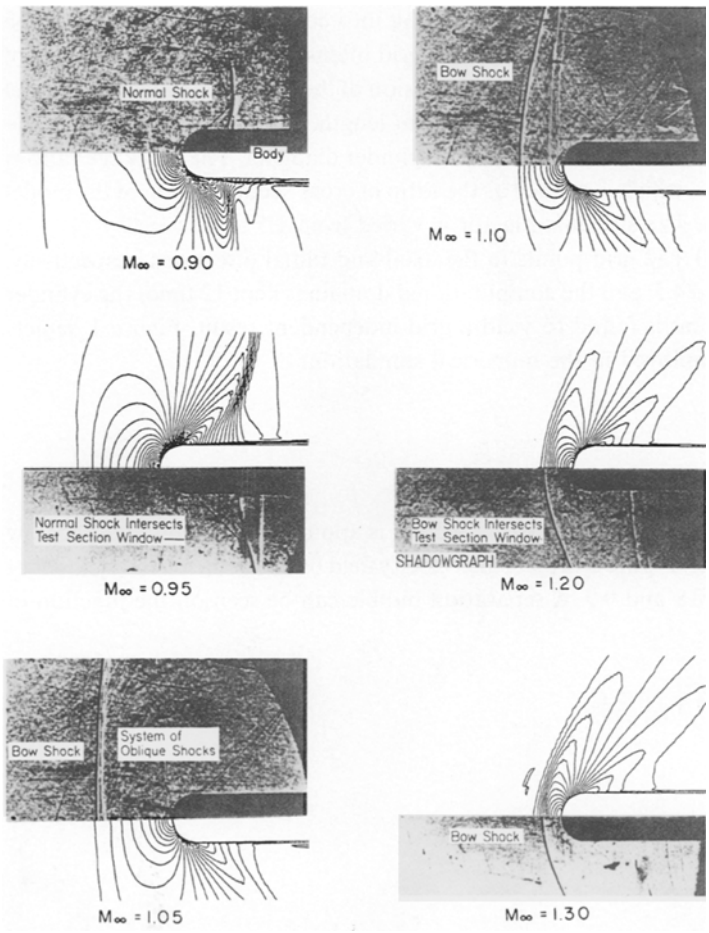

Fig. 3. Flow past hemisphere-cylinder

hemisphere-cylinder. The point of separation and reattachment is indicated in the figure using the symbols S and R, respectively. The formation of the separation bubble due to normal shock wave-turbulent boundary layer interaction on a curved wall is also observed experimentally by Doerffer and Zierep [6]. The application of the Zierep theory on the shock wave-turbulent boundary layer interaction at transonic Mach number is discussed in detail in [7]. Thus, the formation of the separated bubble may be attributed to the shock wave-turbulent boundary layer interaction.

Figure 3 shows the comparison between the density contour plots with the shadowgraph pictures [1] for the Mach number range of 0.9 – 2.0. It can be visualized from the density contours plots that all the essential flow field features of the transonic Mach number such as normal shock and supersonic pocket, and for the supersonic Mach number such as bow shock and system of the oblique shock are very well captured and also compare fairly well with the shadowgraph pictures.

The bow shock standoff distance is calculated employing the following asymptotic formula of Frank and Zierep [8]:

$$\frac{\Delta}{R} = \frac{2(b)^{2/3}}{\left[\dfrac{(M_\infty^2 - 1)}{(\gamma + 1)\, M_\infty^2}\right]^{2/3}} - 1 \tag{8}$$

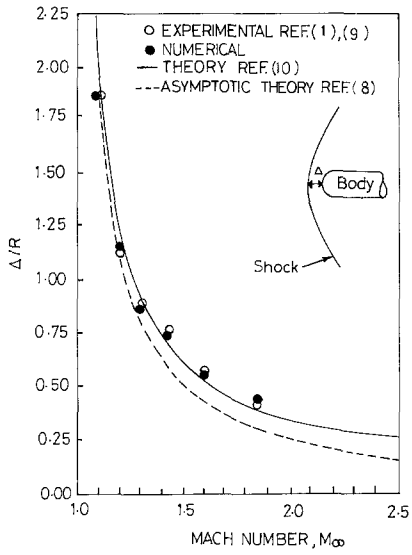

Fig. 4. Comparison of shock stand-off distance between numerical and experimental results

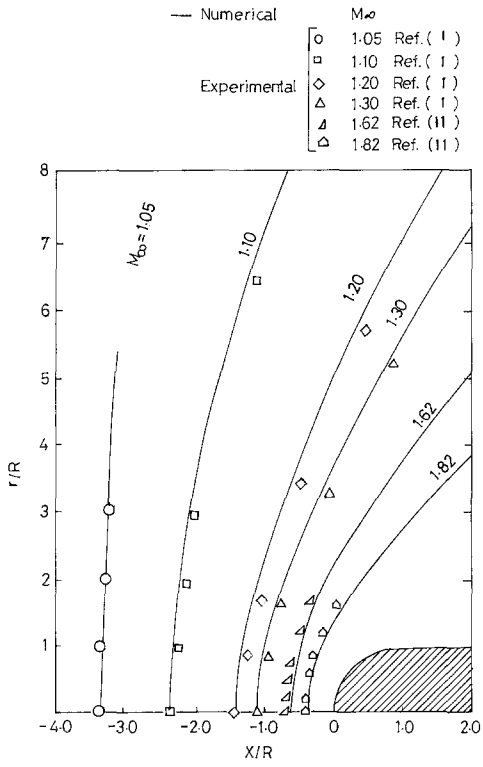

Fig. 5. Comparison of numerical shock position with experiment

where the value of b is taken as 0.14 [8]. The bow shock stand-off distance Δ/R is depicted in Fig. 4. It can be seen from the figure that the comparison of the present numerical result is in agreement with the experimental data [1], [9], asymptotic formula of Frank and Zierep [8] and with the theoretical results of Van Dyke and Gordon [10].

The comparison between numerically computed shock position with the experimental data [1], [11] is depicted in Fig. 5. The agreement between them is satisfactorily. Figure 6 displays an enlarged view of the computed velocity field at supersonic mach number range of 1.4 – 2.0. It can be easily seen that the bow shock moves close to the body with increasing Mach number which is

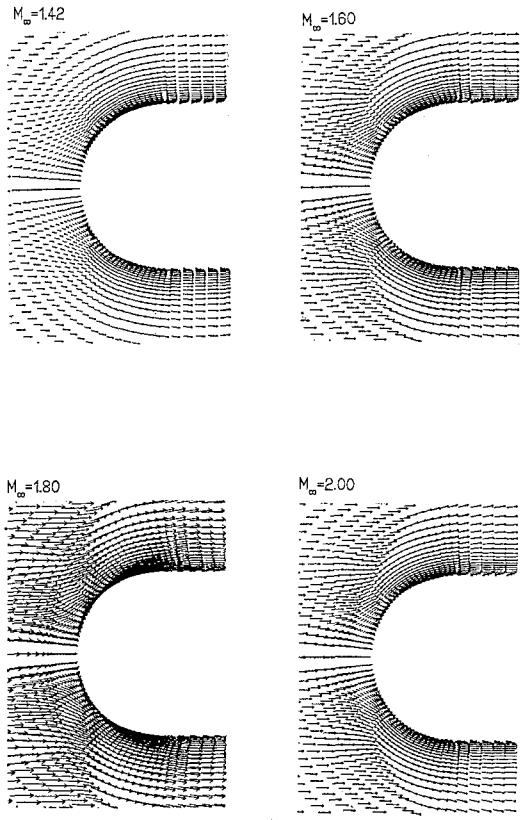

Fig. 6. Computed velocity field and shock position

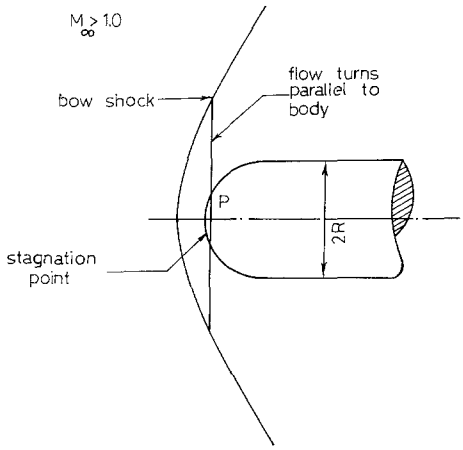

Fig. 7. Schematic sketch of the flow

also coinciding with the shock position as depicted in Fig. 5. It appears from the velocity field that the flow becomes parallel to the body after crossing a line which is perpendicular to the model axis. This line is in the vicinity of the stagnation point of the hemisphere. A schematic sketch of the flow pattern is delineated in Fig. 7 which is constructed based on this observation.

The surface pressure coefficient C_P along the nondimensionalised length x/R of the model is depicted in Fig. 8. In the figures, comparisons are made with the experimental data [1], [12]. A disagreement between numerical and experimental results is found near the hemisphere-cylinder junction at $M_\infty = 0.8 - 1.0$ as can be seen in Fig. 8a. This discrepancy may be

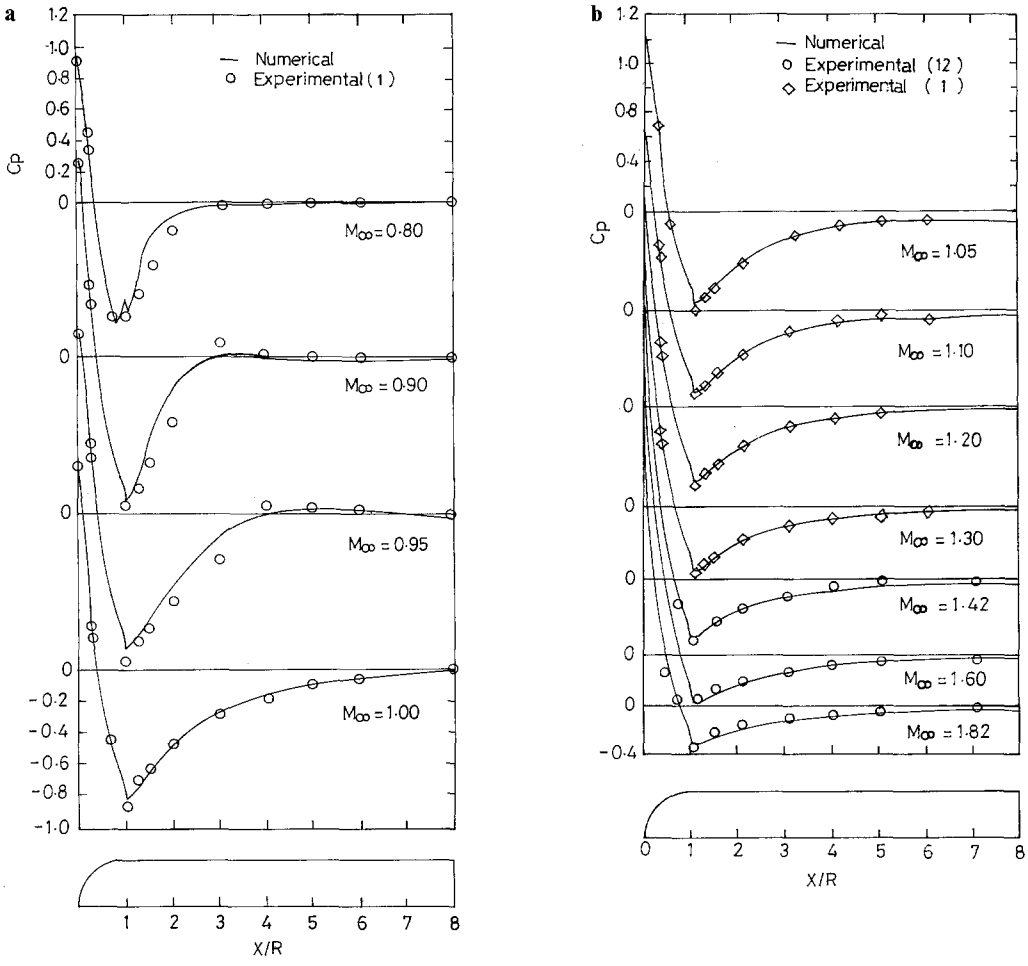

Fig. 8. **a** Variation of pressure coefficient along the body. **b** Variation of pressure coefficient along the body

attributed to a recompression shock following an over expansion zone, and the final local flow resembles a supersonic flow over a compression corner. A satisfactory agreement is observed for all other cases.

4 Conclusions

Viscous flow over the hemisphere-cylinder body has been numerically simulated. All the essential flow field features of the transonic and supersonic Mach number are very well captured and compare satisfactorily with the available shadowgraph pictures. A separation bubble is found to exist on the hemisphere-cylinder in the mach number range of $0.8-0.9$. Comparisons have been made with shock stand-off distance, shock position and pressure distribution and are found in good agreement with the available data. It is observed from the velocity vector plots that the flow appears to become parallel to the model after passing through a line which is perpendicular to the axis and very close to the stagnation point.

Acknowledgement

The author is grateful to Prof. J. Zierep for his valuable suggestions towards the improvement of the present paper.

References

[1] Hsieh, T.: Flow field study about a hemispherical cylinder in transonic and low supersonic Mach number range. AIAA paper 75–83 (1975).
[2] Hsieh, T.: Hemisphere-cylinder in transonic flow, $M_\infty = 0.7-1.0$. AIAA J. **13,** 1411–1413 (1975).
[3] Baldwin, B. S., Lomax, H.: Thin layer approximation and algebraic model for separated turbulent flow. AIAA paper 78–257 (1978).
[4] Jamesons, A., Schmidt, W., Turkel, E.: Numerical solution of Euler equations by finite volume methods using Runge-Kutta time stepping schemes. AIAA paper 81–1259 (1981).
[5] Shang, J. S.: Numerical simulation of wing-fuselage interference. AIAA paper 81–0048 (1981).
[6] Doerffer, P., Zierep, J.: An experimental investigation of the Reynolds number effect on a normal shock wave-turbulent boundary layer interaction on a curved wall. Acta Mech. **73,** 77–73 (1988).
[7] Ramm, H. J.: Fluid dynamics for the study of transonic flow, pp. 152–154. New York: Oxford University Press 1990.
[8] Frank, W., Zierep, J.: Schallnahe Überschallströmung um rotationssymmetrische Körper. Acta Mech. **19,** 277–287 (1974).
[9] Stilp, A.: Strömungsuntersuchungen an Kugeln mit transonischen und supersonischen Geschwindigkeiten in Luft und Frigen-Luftgemischen. Bericht Nr. 10.65, Eckerstrasse 4, Germany (1965).
[10] Van Dyke, M. D., Gordon, H. D.: Supersonic flow past a family of blunt-axisymmetric bodies. NASA TR-R 1 (1959).
[11] Heberle, J. W., Wood, G. P., Gooderum, P. B.: Data on shape and location of detached shock waves on cones and spheres. NACA TN 2000 (1958).
[12] Holder, D. W., Chinneck, A.: The flow past elliptic-nosed cylinder and bodies of revolution in supersonic air stream. Aeronaut. Q. **4,** 317–340 (1954).

Author's address: R. C. Mehta, Aerodynamics Division, Vikram Sarabhai Space Centre, Trivandrum 695 022, India